remote sensing

MDPI

Article

Identifying Heterogeneity in SAR Data with New Test Statistics

Alejandro C. Frery [1,*], Janeth Alpala [2] and Abraão D. C. Nascimento [2]

[1] School of Mathematics and Statistics, Victoria University of Wellington, Wellington 6140, New Zealand
[2] Departamento de Estatística, Universidade Federal de Pernambuco, Recife 50670-901, PE, Brazil; janeth.alpala@ufpe.br (J.A.); abraao@de.ufpe.br (A.D.C.N.)
* Correspondence: alejandro.frery@vuw.ac.nz

Abstract: This paper presents a statistical approach to identify the underlying roughness characteristics in synthetic aperture radar (SAR) intensity data. The physical modeling of this kind of data allows the use of the Gamma distribution in the presence of fully developed speckle, i.e., when there are infinitely many independent backscatterers per resolution cell, and none dominates the return. Such areas are often called "homogeneous" or "textureless" regions. The $\mathcal{G}_I^0$ distribution is also a widely accepted law for heterogeneous and extremely heterogeneous regions, i.e., areas where the fully developed speckle hypotheses do not hold. We propose three test statistics to distinguish between homogeneous and inhomogeneous regions, i.e., between gamma and $\mathcal{G}_I^0$ distributed data, both with a known number of looks. The first test statistic uses a bootstrapped non-parametric estimator of Shannon entropy, providing a robust assessment in uncertain distributional assumptions. The second test uses the classical coefficient of variation (CV). The third test uses an alternative form of estimating the CV based on the ratio of the mean absolute deviation from the median to the median. We apply our test statistic to create maps of p-values for the homogeneity hypothesis. Finally, we show that our proposal, the entropy-based test, outperforms existing methods, such as the classical CV and its alternative variant, in identifying heterogeneity when applied to both simulated and actual data.

Keywords: SAR; heterogeneity; entropy; coefficient of variation; hypothesis tests

check for updates

Citation: Frery, A.C.; Alpala, J.; Nascimento, A.D.C. Identifying Heterogeneity in SAR Data with New Test Statistics. *Remote Sens.* **2024**, *16*, 1973. https://doi.org/10.3390/rs16111973

Academic Editors: Georgia Koukiou and Vassilis Anastassopoulos

Received: 6 May 2024
Revised: 29 May 2024
Accepted: 29 May 2024
Published: 30 May 2024

Copyright: © 2024 by the authors. Licensee MDPI, Basel, Switzerland. This article is an open access article distributed under the terms and conditions of the Creative Commons Attribution (CC BY) license (https://creativecommons.org/licenses/by/4.0/).

1. Introduction

Synthetic Aperture Radar (SAR) technology has become essential for environmental monitoring and disaster management. It provides valuable images under various conditions, including day or night and weather situations [1,2]. However, the effective use of SAR data depends on a thorough understanding of its statistical properties because it is corrupted by speckle. This noise-like interference effect is inherent in SAR data due to the coherent nature of the imaging process [3].

Speckle in intensity format is non-Gaussian. Thus, SAR data require reliable statistical models for accurate processing. The $\mathcal{G}^0$ distribution, which is suitable for SAR data, includes the Gamma law as the limiting case for fully developed speckle [4] and provides flexibility with fewer parameters for analysis.

Our work aims to improve the identification of potential roughness features in SAR intensity data. The physical modeling of SAR data allows the use of the Gamma distribution in the presence of fully developed speckle, where an infinite number of independent backscatterers per resolution unit is assumed, which is commonly referred to as homogeneous regions.

In this context, we present a set of three novel test statistics that aim to distinguish between homogeneous and non-homogeneous returns, particularly between gamma and $\mathcal{G}^0$ distributed data, assuming the number of looks is known. We use properties such as entropy and coefficient of variation.

Entropy is a fundamental concept in information theory with far-reaching applications in pattern recognition, statistical physics, image processing, edge detection and SAR image

analysis [5–9]. Shannon introduced it in 1948 [10] for a random variable to measure information and uncertainty. Shannon entropy is a crucial descriptive parameter in statistics, especially for evaluating data dispersion and performing tests for normality, exponentiality and uniformity [11,12]. Entropy estimation is challenging, especially when the model is unknown; in these cases, non-parametric methods, as those based on spacings [13,14], can be used. This strategy is flexible and robust because it does not enforce a model or parametric constraints. Different roughness levels, which materialize as different models for SAR data, have different entropy values. We designed a bootstrap-improved non-parametric estimator for the Shannon entropy.

The coefficient of variation (CV), introduced in 1896 by Pearson [15], is a relative dispersion measure widely used in various fields of applied statistics, including sampling, biostatistics, medical and biological research, climatology and other fields [16–19]. It facilitates the comparison of variability between different populations and is particularly valuable for relating variables with different units. This is because when the primary purpose is to compare the variations of several variables, the standard deviation can only serve as an adequate measure of variation if all variables are expressed in the same unit of measurement and have identical means. If these conditions are not met, then the CV is the relative measure that is usually used in real applications. The variable with the highest CV value has the largest relative dispersion around the mean value [20]. The coefficient of variation is the primary measure of heterogeneity in SAR data [21,22]. We study two ways of estimating the coefficient of variation.

We devise test statistics based on these three estimators: the classical coefficient of variation, a robust version, and the Shannon entropy estimator. We apply these test statistics to generate maps of evidence of homogeneity that reveal different types of targets in the SAR data. We show that our proposed method is superior to existing approaches with simulated data and SAR images.

The article is structured as follows: Section 2 deals with statistical modeling and entropy estimation for intensity SAR data. Section 3 outlines hypothesis tests based on non-parametric entropy and coefficients of variation estimators. In Section 4, we present experimental results. Finally, we draw conclusions in Section 5.

We used Rmarkdown https://andrewbtran.github.io/NICAR/2017/reproducibility-rmarkdown/rmarkdown.html#reproducible_research (accessed on 30 April 2024) to produce this work. It is fully reproducible because it contains the code and data needed to replicate it. The Supplementary Materials information points to the repository from where it can be downloaded.

2. Background

2.1. Statistical Modeling of Intensity SAR Data

The primary models for intensity SAR data include the Gamma and $\mathcal{G}_I^0$ distributions [23]. The first is suitable for fully developed speckle and is a limiting case of the second model. This is interesting due to its versatility in accurately representing regions with different roughness properties [24]. We denote $Z \sim \Gamma_{\mathrm{SAR}}(L, \mu)$ and $Z \sim \mathcal{G}_I^0(\alpha, \gamma, L)$ to indicate that Z follows the distributions characterized by the respective probability density functions (pdfs):

$$f_Z(z; L, \mu \mid \Gamma_{\mathrm{SAR}}) = \frac{L^L}{\Gamma(L)\mu^L} z^{L-1} \exp\{-Lz/\mu\} \mathbb{1}_{\mathbb{R}_+}(z) \tag{1}$$

and

$$f_Z(z; \alpha, \gamma, L \mid \mathcal{G}_I^0) = \frac{L^L \Gamma(L-\alpha)}{\gamma^\alpha \Gamma(-\alpha)\Gamma(L)} \cdot \frac{z^{L-1}}{(\gamma + Lz)^{L-\alpha}} \mathbb{1}_{\mathbb{R}_+}(z), \tag{2}$$

where $\mu > 0$ is the mean, $\gamma > 0$ is the scale, $\alpha < 0$ measures the roughness, $L \geq 1$ is the number of looks (either nominal or estimated, thus not restricted to integer values), $\Gamma(\cdot)$ is the gamma function, and $\mathbb{1}_A(z)$ is the indicator function of the set A.

The rth order moments of the $\mathcal{G}_I^0$ model are

$$E(Z^r \mid \mathcal{G}_I^0) = \left(\frac{\gamma}{L}\right)^r \frac{\Gamma(-\alpha - r)}{\Gamma(-\alpha)} \cdot \frac{\Gamma(L + r)}{\Gamma(L)}, \tag{3}$$

provided $\alpha < -r$, and they are infinite otherwise. Therefore, assuming $\alpha < -1$, its expected value is

$$\mu = \left(\frac{\gamma}{L}\right) \frac{\Gamma(-\alpha - 1)}{\Gamma(-\alpha)} \cdot \frac{\Gamma(L + 1)}{\gamma(L)} = -\frac{\gamma}{\alpha + 1}. \tag{4}$$

Although the $\mathcal{G}_I^0$ distribution is defined by the parameters α and γ, in the SAR literature [25], the texture α and the mean μ are usually used. Reparametrizing (2) with μ, and denoting this model as G_I^0, we obtain the following:

$$f_Z(z; \mu, \alpha, L \mid G_I^0) = \frac{L^L \Gamma(L - \alpha)}{[-\mu(\alpha + 1)]^\alpha \Gamma(-\alpha)\Gamma(L)} \frac{z^{L-1}}{[-\mu(\alpha + 1) + Lz]^{L-\alpha}}. \tag{5}$$

2.2. The Shannon Entropy

The parametric representation of Shannon entropy for a system described by a continuous random variable is

$$H(Z) = -\int_{-\infty}^{\infty} f(z) \ln f(z) \, \mathrm{d}z, \tag{6}$$

here, $f(\cdot)$ is the pdf that characterizes the distribution of the real-valued random variable Z.

Using (6), we obtain the Shannon entropy of Γ_{SAR} in (1) and G_I^0 in (5):

$$H_{\Gamma_{\text{SAR}}}(L, \mu) = L - \ln L + \ln \Gamma(L) + (1 - L)\psi^{(0)}(L) + \ln \mu, \tag{7}$$

$$\begin{aligned} H_{G_I^0}(\mu, \alpha, L) = {} & L - \ln L + \ln \Gamma(L) + (1 - L)\psi^{(0)}(L) + \ln \mu - \ln \Gamma(L - \alpha) \\ & + (L - \alpha)\psi^{(0)}(L - \alpha) - (1 - \alpha)\psi^{(0)}(-\alpha) + \ln(-1 - \alpha) + \ln \Gamma(-\alpha) - L, \end{aligned} \tag{8}$$

where $\psi^{(0)}(\cdot)$ is the digamma function. Figure 1 shows the entropy of G_I^0 as a function of μ when $\alpha \in \{-\infty, -20, -8, -3\}$. Notice that it converges to the entropy of Γ_{SAR} when $\alpha \to -\infty$, as expected. The more heterogeneous (large α values) the SAR region is, the larger the entropy (or degree of disorder) is.

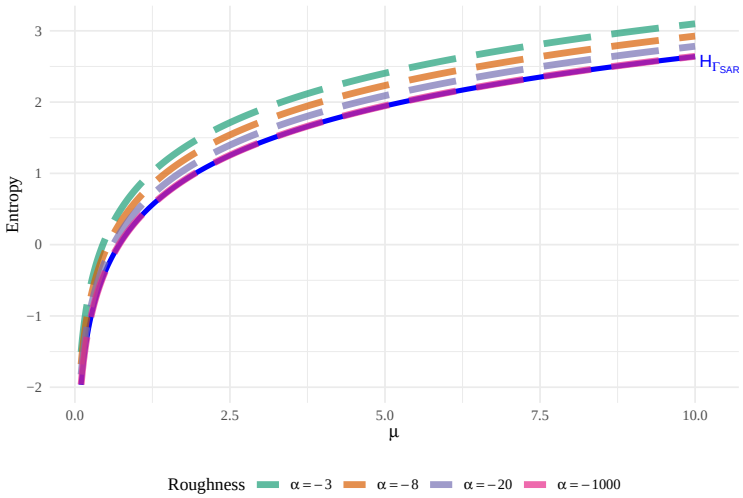


Figure 1. $H_{G_I^0}$ converges to the $H_{\Gamma_{\text{SAR}}}$ when $\alpha \to -\infty$, with $L = 8$.

Appendix A provides the proof of the convergence of $H_{G_I^0}(\mu, \alpha, L)$ to $H_{\Gamma_{SAR}}(L, \mu)$ when $\alpha \to -\infty$.

2.3. Estimation of the Shannon Entropy

The problem of the non-parametric estimation of $H(Z)$ has been studied by many authors, including [11,26–28]. Their proposals use estimators based on differences between order statistics: spacings.

Vasicek [26] introduced one of the first non-parametric estimators based on spacings. Under the assumption that $\boldsymbol{Z} = (Z_1, Z_2, \ldots, Z_n)$ is a random sample from the distribution $F(z)$, the estimator is defined as

$$\widehat{H}_{\mathrm{V}}(\boldsymbol{Z}) = \frac{1}{n}\sum_{i=1}^{n} \ln\Big[\frac{n}{2m}\Big(Z_{(i+m)} - Z_{(i-m)}\Big)\Big],$$

where $m < n/2$ is a positive integer, $Z_{(1)} \leq Z_{(2)} \leq \cdots \leq Z_{(n)}$ are the order statistics, and $Z_{(i+m)} - Z_{(i-m)}$ is the m-spacing, in which $Z_{(i)} = Z_{(1)}$ if $i < 1$, $Z_{(i)} = Z_{(n)}$ if $i > n$.

Several authors have explored adaptations to Vasicek's estimator. We consider three estimators known for their superior performance [24]:

- Correa [27]:

$$\widehat{H}_{\mathrm{C}}(\boldsymbol{Z}) = -\frac{1}{n}\sum_{i=1}^{n} \log \frac{\sum_{j=i-m}^{i+m}(j-i)\Big(Z_{(j)} - \overline{Z}_{(i)}\Big)}{n\sum_{j=i-m}^{i+m}\Big(Z_{(j)} - \overline{Z}_{(i)}\Big)^2}, \tag{9}$$

  where $\overline{Z}_{(i)} = (2m+1)^{-1}\sum_{j=i-m}^{i+m} Z_{(j)}$, $m < \frac{n}{2}$, $Z_{(i)} = Z_{(1)}$ for $i < 1$ and $Z_{(i)} = Z_{(n)}$ for $i > n$. Based on simulations, he showed that his estimator has a smaller mean square error than Vasicek's approach.

- Ebrahimi et al. [29]:

$$\widehat{H}_{\mathrm{E}}(\boldsymbol{Z}) = \frac{1}{n}\sum_{i=1}^{n} \log\Big[\frac{n}{c_i m}\Big(Z_{(i+m)} - Z_{(i-m)}\Big)\Big], \tag{10}$$

  where

$$c_i = \begin{cases} 1 + (i-1)/m & \text{if} \quad 1 \leq i \leq m, \\ 2 & \text{if} \quad m+1 \leq i \leq n-m, \\ 1 + (n-i)/m & \text{if} \quad n-m+1 \leq i \leq n. \end{cases}$$

- Al-Omari [30]:

$$\widehat{H}_{\mathrm{AO}}(\boldsymbol{Z}) = \frac{1}{n}\sum_{i=1}^{n} \log\Big[\frac{n}{\omega_i m}\Big(Z_{(i+m)} - Z_{(i-m)}\Big)\Big],$$

  where

$$\omega_i = \begin{cases} 3/2 & \text{if} \quad 1 \leq i \leq m, \\ 2 & \text{if} \quad m+1 \leq i \leq n-m, \\ 3/2 & \text{if} \quad n-m+1 \leq i \leq n, \end{cases}$$

  in which $Z_{(i-m)} = Z_{(1)}$ for $i \leq m$, and $Z_{(i+m)} = Z_{(n)}$ for $i \geq n-m$.

These estimators are asymptotically consistent, i.e., they converge in probability to the true value when $m, n \to \infty$ and $m/n \to 0$. However, we will use improved bootstrap-improved versions because we need them to perform well with small samples.

2.4. Enhanced Estimators with Bootstrap

We use the bootstrap technique to refine the accuracy of non-parametric entropy estimators. In this approach, new datasets are generated by replicate sampling from an existing dataset [31].

Let us assume that the non-parametric entropy estimator $\widehat{H} = \widehat{\theta}(\boldsymbol{Z})$ is inherently biased, i.e.,

$$\text{Bias}\left(\widehat{\theta}(\boldsymbol{Z})\right) = E\left[\widehat{\theta}(\boldsymbol{Z})\right] - \theta \neq 0. \tag{11}$$

Our bootstrap-improved estimator is of the following form:

$$\widetilde{H} = 2\widehat{\theta}(\boldsymbol{Z}) - \frac{1}{B}\sum_{b=1}^{B}\widehat{\theta}_b(\boldsymbol{Z}^{(b)}),$$

where B is the number of observations obtained by resampling from $\boldsymbol{Z}$ with replacement. Applying this methodology, the original estimators of Correa, Ebrahimi and Al-Omari are now referred to as the proposed bootstrap-improved versions: $\widetilde{H}_{\mathrm{C}}$, $\widetilde{H}_{\mathrm{E}}$, and $\widetilde{H}_{\mathrm{AO}}$, respectively.

We analyzed the performance of these estimators with a Monte Carlo study: 1000 samples from the Γ_{SAR} distribution of size $n \in \{9, 25, 49, 81, 121\}$ with $\mu \in \{1, 10\}$ and $L = 5$. The results are consistent with other situations. We used $B = 200$ bootstrap samples and the heuristic spacing $m = \lfloor \sqrt{n} + 0.5 \rfloor$, as recommended in the literature.

In Figure 2, we show the bias and mean squared error (MSE) of the original non-parametric entropy estimators and their respective bootstrap-enhanced versions. Bootstrap-enhanced estimators have smaller bias and MSE, especially for sample sizes below 81. The results of the simulation can be found in Table 1.

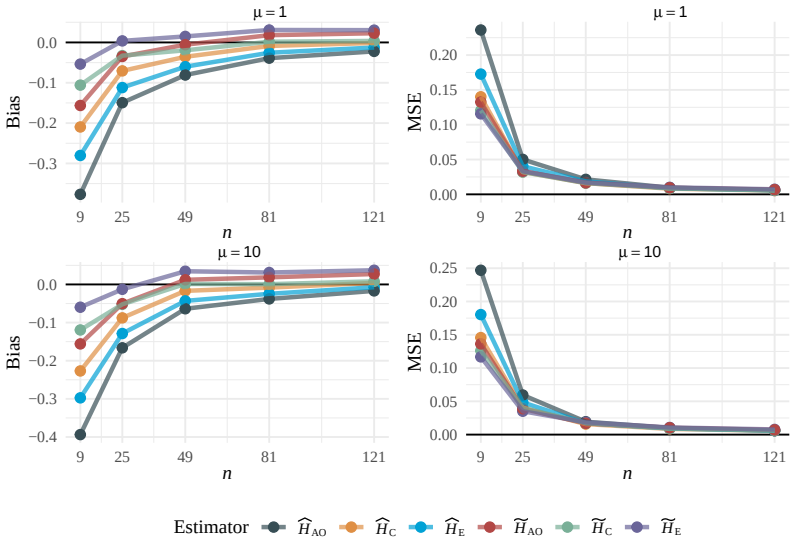


Figure 2. Bias and MSE of the entropy estimators for the Γ_{SAR} with $L = 5$.

Table 1. Bias and MSE of the entropy estimators for the Γ_{SAR} with $L = 5$.

		Bias						MSE					
μ	n	$\widehat{H}_{\mathrm{C}}$	$\widehat{H}_{\mathrm{E}}$	$\widehat{H}_{\mathrm{AO}}$	$\widetilde{H}_{\mathrm{C}}$	$\widetilde{H}_{\mathrm{E}}$	$\widetilde{H}_{\mathrm{AO}}$	$\widehat{H}_{\mathrm{C}}$	$\widehat{H}_{\mathrm{E}}$	$\widehat{H}_{\mathrm{AO}}$	$\widetilde{H}_{\mathrm{C}}$	$\widetilde{H}_{\mathrm{E}}$	$\widetilde{H}_{\mathrm{AO}}$
1	9	−0.210	−0.280	−0.377	−0.106	−0.054	−0.156	0.140	0.173	0.236	0.121	0.116	0.133
	25	−0.071	−0.112	−0.149	−0.033	0.004	−0.035	0.032	0.040	0.050	0.032	0.033	0.033
	49	−0.036	−0.060	−0.081	−0.020	0.015	−0.006	0.016	0.019	0.021	0.016	0.017	0.017
	81	−0.009	−0.026	−0.039	0.002	0.031	0.018	0.008	0.009	0.010	0.009	0.010	0.009
	121	−0.001	−0.013	−0.022	0.004	0.030	0.023	0.005	0.006	0.006	0.006	0.007	0.007
10	9	−0.227	−0.297	−0.394	−0.119	−0.060	−0.156	0.146	0.180	0.247	0.126	0.117	0.136
	25	−0.088	−0.129	−0.166	−0.052	−0.013	−0.050	0.040	0.048	0.059	0.040	0.035	0.039
	49	−0.017	−0.043	−0.064	0.001	0.035	0.012	0.016	0.017	0.019	0.018	0.019	0.017
	81	−0.008	−0.025	−0.038	0.001	0.031	0.019	0.009	0.009	0.010	0.009	0.011	0.010
	121	0.004	−0.007	−0.017	0.008	0.037	0.027	0.006	0.006	0.006	0.006	0.008	0.007

2.5. Coefficient of Variation and a Robust Alternative

The population CV is defined as a ratio of the population standard deviation (σ) to the population mean (μ):

$$\mathrm{CV} = \frac{\sigma}{\mu}, \quad \mu \neq 0. \tag{12}$$

The CV can be easily estimated as the ratio of the sample mean to the sample standard deviation.

We explore a robust alternative to estimate the CV, as described by [32]: the ratio between the mean absolute deviation from the median (MnAD) and the median, two well-known robust measures of scale and location, respectively. The sample version for the MnAD is defined as $n^{-1}\sum_{i=1}^{n}|x_i - \widehat{Q}_2|$, where $\widehat{Q}_2$ is an estimate for the median of the population, for example, the sample median.

3. Hypothesis Testing

We aim to test the following hypotheses:

$$\begin{cases} \mathcal{H}_0: \text{ The data come from the } \Gamma_{\mathrm{SAR}} \text{ law,} \\ \mathcal{H}_1: \text{ The data come from the } G_I^0 \text{ distribution.} \end{cases}$$

We are testing the hypothesis that the data are fully developed speckle versus the alternative of data with roughness. As for the parametric problem, once it is not possible to define the hypothesis $\mathcal{H}_0 = \alpha = -\infty$, it is impossible to solve this problem with parametric inference alternatives (such as likelihood ratio, score, gradient, and Wald hypothesis test). The proposed tests to solve this physical problem in SAR systems are described below.

3.1. The Proposed Test Based on Non-Parametric Entropy

For a random sample $\boldsymbol{Z} = (Z_1, Z_2, \ldots, Z_n)$ from a distribution $\mathcal{D}$, a test statistic is proposed. It is based on an empirical distribution that arises from the difference between non-parametrically estimated entropies $\widetilde{H}(\boldsymbol{Z})$ and the analytical entropy of Γ_{SAR} (7) evaluated at the logarithm of the sample mean, where $L \geq 1$ is known.

Hence, the entropy-based test statistic is defined as

$$S(\boldsymbol{Z}; L) = \widetilde{H}(\boldsymbol{Z}) - \left[H_{\Gamma_{\mathrm{SAR}}}(L) + \ln \overline{\boldsymbol{Z}}\right]. \tag{13}$$

This test statistic aims to assess the behavior of the data under the null hypothesis using the empirical distribution. If the data represent fully developed speckle, the density should center around zero, i.e., $S(\boldsymbol{Z}; L) \approx 0$. Otherwise, the empirical distribution would shift from zero under the alternative hypothesis, suggesting significant differences and heterogeneous clutter.

The comparison between the bootstrap-improved estimators is shown in Table 2, where the test accuracy under the null hypothesis is presented alongside running times. The test accuracy is evaluated through 1000 simulated samples of different sizes with each size replicated 100 times using bootstrap resampling.

The processing time is an important feature, especially considering the application of these estimators to large datasets of SAR images, as seen in Section 4.

As visible from Table 2, the accuracy of the test results across the three estimators shows similarities in specific sample sizes. However, practical scenarios in SAR image processing often involve small sample sizes, which are typically obtained over windows of size 7×7. It is also noteworthy that the $\widetilde{H}_{\mathrm{AO}}$ estimator exhibited the shortest processing time, which was followed by $\widetilde{H}_{\mathrm{E}}$ and $\widetilde{H}_{\mathrm{C}}$. Considering this aspect, we select the $\widetilde{H}_{\mathrm{AO}}$ estimator for subsequent simulations. Henceforth, the test statistical (13) will be denoted as $S_{\widetilde{H}_{\mathrm{AO}}}(\boldsymbol{Z}; L)$.

We now verify the normality of the data generated by the $S_{\widetilde{H}_{\mathrm{AO}}}(\boldsymbol{Z}; L)$ test. Figure 3 shows the empirical densities obtained by applying the $S_{\widetilde{H}_{\mathrm{AO}}}(\boldsymbol{Z}; L)$ test to different sample

sizes drawn from the Γ_{SAR} distribution, where L takes values $\{3, 5, 8, 11\}$ and $\mu = 1$. Additionally, Table 3 summarizes the main descriptive statistics, including mean, standard deviation (SD), variance (Var), skewness (SK), excessive kurtosis (EK) and Anderson–Darling p values for normality. Results with p values greater than 0.05 do not indicate a violation of the normality assumption. A low variance, skewness, and excessive kurtosis of almost zero indicate limited dispersion, asymmetry, and a light tail. Normal Q–Q plots confirm no evidence against a normal distribution, as shown in Figure 4.

Table 2. Tests accuracy and processing time for each bootstrap-improved estimator.

Estimator	L	n	$S(Z;L)$	Time (s)
$\widetilde{H}_{C}$	2	25	−0.00152	22.53
		49	0.00515	40.35
		81	0.00625	63.93
		121	0.00751	97.06
	8	25	−0.04332	22.25
		49	−0.01659	33.42
		81	−0.00393	50.94
		121	0.00261	97.35
$\widetilde{H}_{E}$	2	25	0.02204	4.66
		49	0.03452	5.55
		81	0.03195	6.89
		121	0.03012	7.90
	8	25	0.00801	4.81
		49	0.01654	5.43
		81	0.03036	6.38
		121	0.03137	7.46
$\widetilde{H}_{AO}$	2	25	−0.01935	4.61
		49	0.00786	5.19
		81	0.01995	6.70
		121	0.01741	7.41
	8	25	−0.04020	4.74
		49	0.00047	5.35
		81	0.01176	6.21
		121	0.02019	7.48

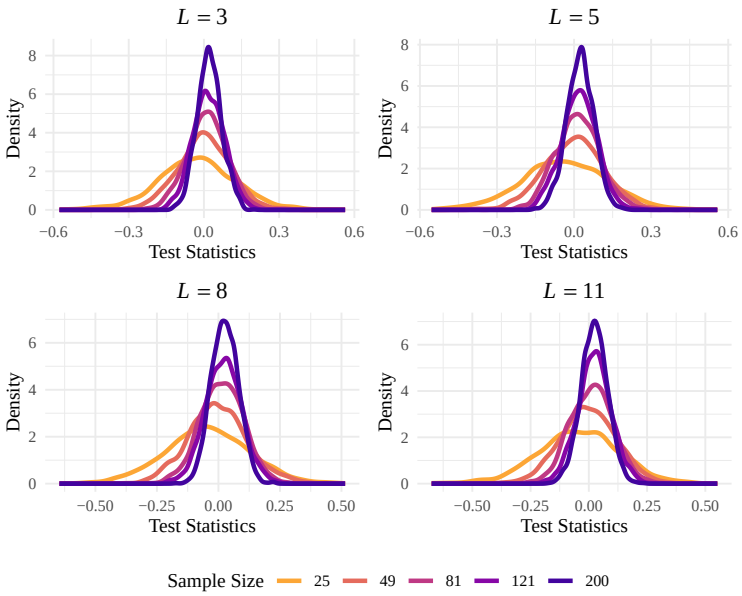


Figure 3. Empirical densities obtained from $S_{\widetilde{H}_{AO}}(\mathbf{Z};L)$ test under the null hypothesis.

Table 3. Descriptive analysis of $S_{\widetilde{H}_{\mathrm{AO}}}(\mathbf{Z}; L)$, with $L \in \{3, 5, 8, 11\}$ and $\mu = 1$.

L	n	Mean	SD	Var	SK	EK	p-Value
3	25	−0.0280	0.1547	0.0239	−0.0076	0.4734	0.0022
	49	−0.0003	0.1053	0.0111	−0.0562	0.2610	0.0582
	81	0.0124	0.0796	0.0063	−0.0124	0.0536	0.5278
	121	0.0187	0.0630	0.0040	0.0337	−0.1826	0.5894
	200	0.0215	0.0490	0.0024	0.0625	−0.0473	0.0860
5	25	−0.0379	0.1669	0.0278	0.0007	0.1420	0.3267
	49	−0.0015	0.1150	0.0132	−0.1025	0.1998	0.2582
	81	0.0145	0.0869	0.0075	0.1008	0.5297	0.1121
	121	0.0198	0.0687	0.0047	0.0127	0.0222	0.2919
	200	0.0236	0.0529	0.0028	−0.0467	0.0977	0.3346
8	25	−0.0464	0.1680	0.0282	−0.0121	0.0980	0.6477
	49	−0.0031	0.1202	0.0144	0.1282	0.2000	0.0038
	81	0.0137	0.0883	0.0078	−0.0279	0.2554	0.5567
	121	0.0200	0.0738	0.0055	−0.0089	0.0686	0.7502
	200	0.0260	0.0546	0.0030	0.0716	−0.0349	0.3771
11	25	−0.0442	0.1735	0.0301	−0.1422	0.2413	0.0981
	49	−0.0019	0.1201	0.0144	−0.0503	0.1464	0.9576
	81	0.0127	0.0917	0.0084	−0.0172	0.0333	0.3179
	121	0.0239	0.0729	0.0053	−0.0127	0.2102	0.0596
	200	0.0234	0.0572	0.0033	−0.0233	0.1072	0.6740

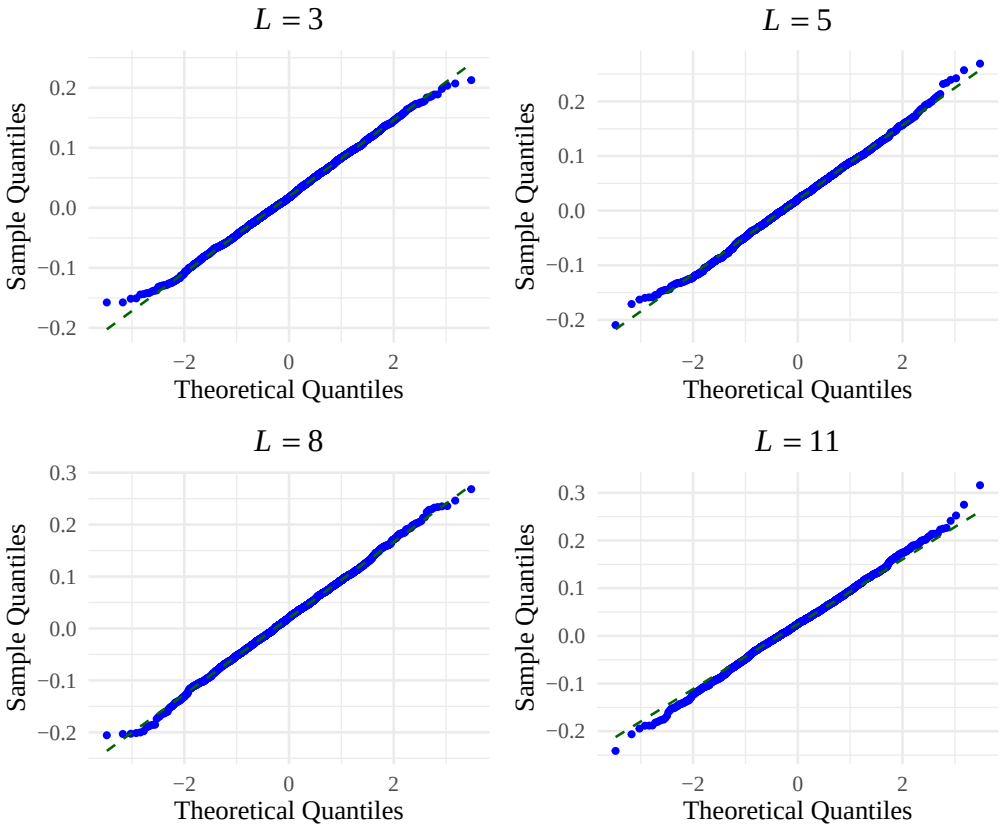


Figure 4. Normal Q–Q plots for $n = 121$. The dashed green lines in the Q–Q plots represent theoretical expected quantiles for a normal distribution. Variations in the scales of the axes reflect differences in the range of values across datasets.

After checking the data's normality, we examined the proposed test's abilities in terms of size (Type I error rate) and power (probability of correctly rejecting the null hypothesis when the alternative hypothesis is true).

Under $\mathcal{H}_0$, the distribution of the test statistic is asymptotically normal. Therefore, the p values are calculated as $2\Phi(-|\varepsilon|)$, where Φ is the standard Gaussian cumulative distribution function, and ε is the standardized test statistic given by

$$\varepsilon = \frac{\widetilde{H}_{\mathrm{AO}}(\boldsymbol{Z}) - \left[H_{\Gamma_{\mathrm{SAR}}}(L) + \ln \overline{\boldsymbol{Z}}\right]}{\widehat{\sigma}}.$$

We conducted the test at nominal significance levels of 1 %, 5 %, and 10 %. These levels represent the probability of rejecting the null hypothesis when it is actually true (Type I error rates). To verify that the test maintains these nominal levels, we performed 1000 simulations under the null hypothesis (Γ_{SAR} distribution) with different sample sizes and values of L, and $\mu = 1$. In all cases, the observed Type I error rates were consistent with the nominal levels, indicating that the test maintains the specified significance levels.

We also evaluated the test's power by performing 1000 simulations under the alternative hypothesis (G_I^0 distribution) with $\mu = 1$ and $\alpha = -2$. The power generally improves with increasing sample size and number of looks. The results are shown in Table 4.

Table 4. Size and power of the $S_{\widetilde{H}_{\mathrm{AO}}}(\boldsymbol{Z})$ test statistic.

		Size			**Power**		
L	***n***	**1%**	**5%**	**10%**	**1%**	**5%**	**10%**
3	25	0.0160	0.0620	0.1070	0.6900	0.8450	0.8340
	49	0.0100	0.0480	0.0960	0.6890	0.8920	0.8480
	81	0.0120	0.0490	0.1080	0.6260	0.8750	0.8540
	121	0.0090	0.0690	0.1190	0.5680	0.8620	0.8230
5	25	0.0210	0.0660	0.1130	0.9120	0.9620	0.9880
	49	0.0100	0.0460	0.1080	0.9470	0.9820	0.9960
	81	0.0120	0.0560	0.1070	0.9580	0.9900	0.9960
	121	0.0150	0.0640	0.1150	0.9420	0.9780	0.9950
8	25	0.0210	0.0650	0.1080	0.9930	0.9950	0.9970
	49	0.0060	0.0470	0.0860	0.9980	1.0000	0.9970
	81	0.0120	0.0490	0.1000	0.9930	0.9980	0.9990
	121	0.0150	0.0650	0.1220	0.9970	0.9990	0.9980
11	25	0.0130	0.0610	0.1000	0.9990	0.9990	0.9990
	49	0.0100	0.0450	0.0920	0.9980	0.9990	0.9990
	81	0.0170	0.0530	0.1050	1.0000	1.0000	1.0000
	121	0.0160	0.0680	0.1180	0.9980	1.0000	0.9980

3.2. The Proposed Test Based on Coefficient of Variation and a Robust Alternative

In addition to the $S_{\widetilde{H}_{\mathrm{AO}}}(\boldsymbol{Z}; L)$ test, we also propose a test statistic based on the classical CV. This test statistic is defined as follows:

$$T_{\mathrm{CV}} = \frac{S}{\overline{Z}}, \tag{14}$$

where S and $\overline{Z}$ are the sample standard deviation and mean, respectively.

Similarly, we use another test statistic based on the ratio of the MnAD to the median. This statistic is given by

$$T_{\mathrm{CV}_{\mathrm{MnAD}}} = \frac{\mathrm{MnAD}}{\mathrm{Median}}. \tag{15}$$

We proceed to identify suitable models for these estimators of the CV and then form test statistics.

The situations in which the use of CV and $\mathrm{CV}_{\mathrm{MnAD}}$ may be appropriate, i.e., when the observations are positive, the log-normal (LN) and the inverse Gaussian distribution (IG) are often more appropriate than the Gamma and Weibull distributions [33,34].

It is shown that the IG distribution is well approximated by the log-normal distribution, which means that the IG distribution also does not share the problem of the non-existence of a fixed-width confidence interval with the Gaussian case [35].

The biparametric LN distribution has the following density:

$$f_Z(z;\mu_{\mathrm{LN}},\sigma_{\mathrm{LN}}) = \frac{1}{\sigma_{\mathrm{LN}} z\sqrt{2\pi}} \exp\left\{-\frac{(\ln z-\mu_{\mathrm{LN}})^2}{2\sigma_{\mathrm{LN}}^2}\right\} \mathbb{1}_{\mathbb{R}_+}(z), \tag{16}$$

where μ_{LN} is any real number, and σ_{LN} is positive.

3.3. Model Selection Criterion

We used the Akaike information criterion (AIC) and the Bayesian information criterion (BIC) to select the best-fitting distribution.

The AIC deals with the trade-off between the goodness-of-fit and the model's simplicity in terms of the number of model parameters [36]. The model or distribution with the lowest value of AIC is chosen to be the best. The BIC assesses the goodness-of-fit of a distribution or model, but it avoids overfitting by penalizing additional degrees of freedom [37]. The model with the lowest BIC value is chosen as the best.

The AIC and BIC results in Tables 5–8 indicate that the CV and $\mathrm{CV}_{\mathrm{MnAD}}$ data from different distributed Γ_{SAR} and G_I^0 synthetic sample sizes match the properties of an LN distribution. It is important to note that this conclusion was drawn empirically based on a dictionary of analytically tractable distributions and is well-defined under biparametric, unimodal, asymmetric, and positive distributions.

Figures 5–8 show empirical and fitted density plots, Q–Q plots, P–P plots, as well as empirical and fitted cumulative distribution functions. They provide qualitative sources that confirm that the LN distribution is the most appropriate distribution. As expected, both test statistics work well under the null hypothesis. Under the alternative hypothesis, the P–P plot shows that $\mathrm{CV}_{\mathrm{MnAD}}$ is more robust than CV, although both statistics suffer from the tail effect caused by the distributed G_I^0 data.

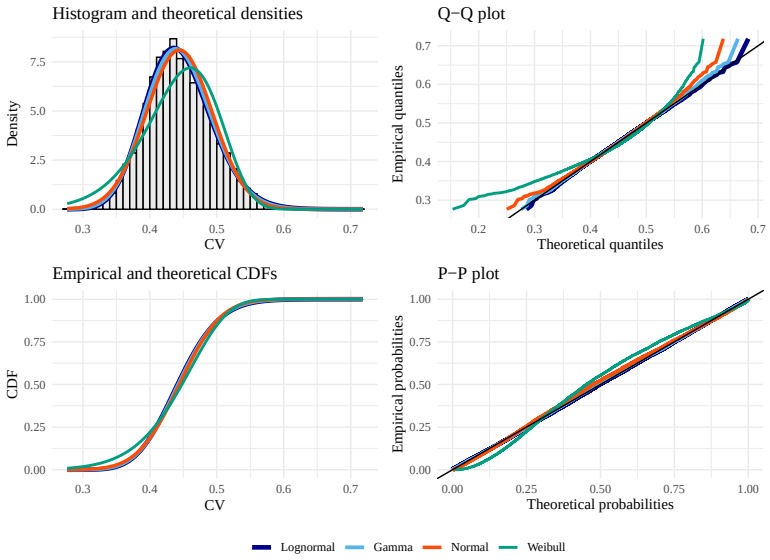


Figure 5. Goodness-of-fit plots for evaluating the best distribution with CV data from Γ_{SAR} (under the null hypothesis) with $n = 49$, $L = 5$, and $\mu = 1$.

Table 5. AIC and BIC values for evaluating the best distribution with CV data from Γ_{SAR}.

Criterion	*n*	Normal	Lognormal	Gamma	Weibull	Inverse Gaussian
AIC	25	−38,031.9	−38,266.7	−38,311.8	−36,413.2	−38,261.6
	49	−47,698.2	−47,913.7	−47,905.6	−45,554.0	−47,911.6
	81	−55,382.1	−55,494.7	−55,494.9	−53,220.4	−55,493.8
	121	−61,344.9	−61,470.8	−61,453.8	−58,876.0	−61,470.5
BIC	25	−38,016.7	−38,251.5	−38,296.6	−36,398.0	−38,246.4
	49	−47,683.0	−47,898.5	−47,890.4	−45,538.7	−47,896.4
	81	−55,366.9	−55,479.5	−55,479.6	−53,205.2	−55,478.6
	121	−61,329.7	−61,455.6	−61,438.6	−58,860.8	−61,455.2

Table 6. AIC and BIC values for evaluating the best distribution with CV data from G_I^0.

Criterion	*n*	Normal	Lognormal	Gamma	Weibull	Inverse Gaussian
AIC	25	8254.04	2186.31	3628.40	8383.58	2257.63
	49	8821.79	1689.03	3483.10	9533.53	1835.29
	81	8525.81	866.29	2853.31	9822.48	1057.91
	121	8708.81	131.86	2341.06	10,506.49	398.53
BIC	25	8269.27	2201.54	3643.63	8398.81	2272.86
	49	8837.02	1704.26	3498.33	9548.76	1850.52
	81	8541.04	881.52	2868.55	9837.72	1073.14
	121	8724.04	147.09	2356.29	10,521.72	413.76

Table 7. AIC and BIC values for evaluating the best distribution with CV_{MnAD} data from Γ_{SAR}.

Criterion	*n*	Normal	Lognormal	Gamma	Weibull	Inverse Gaussian
AIC	25	−38,375.56	−39,147.85	−39,066.29	−36,652.49	−39,143.61
	49	−48,386.11	−48,795.32	−48,745.48	−46,240.91	−48,793.83
	81	−56,072.87	−56,322.32	−56,290.02	−53,836.04	−56,322.12
	121	−62,217.14	−62,394.77	−62,369.32	−59,861.80	−62,394.57
BIC	25	−38,360.32	−39,132.62	−39,051.05	−36,637.26	−39,128.38
	49	−48,370.87	−48,780.09	−48,730.25	−46,225.67	−48,778.60
	81	−56,057.64	−56,307.09	−56,274.79	−53,820.81	−56,306.89
	121	−62,201.91	−62,379.54	−62,354.09	−59,846.56	−62,379.33

Table 8. AIC and BIC values for evaluating the best distribution with CV_{MnAD} data from G_I^0.

Criterion	*n*	Normal	Lognormal	Gamma	Weibull	Inverse Gaussian
AIC	25	−13,302.39	−15,575.23	−15,158.42	−11,933.35	−15,565.03
	49	−23,265.27	−24,529.72	−24,284.47	−20,986.94	−24,522.28
	81	−29,908.19	−30,960.38	−30,747.90	−25,233.41	−30,946.54
	121	−36,496.78	−37,128.07	−36,991.41	−32,366.52	−37,123.20
BIC	25	−13,287.16	−15,559.99	−15,143.19	−11,918.12	−15,549.80
	49	−23,250.04	−24,514.48	−24,269.24	−20,971.71	−24,507.05
	81	−29,892.96	−30,945.15	−30,732.67	−25,218.17	−30,931.31
	121	−36,481.55	−37,112.84	−36,976.18	−32,351.28	−37,107.97

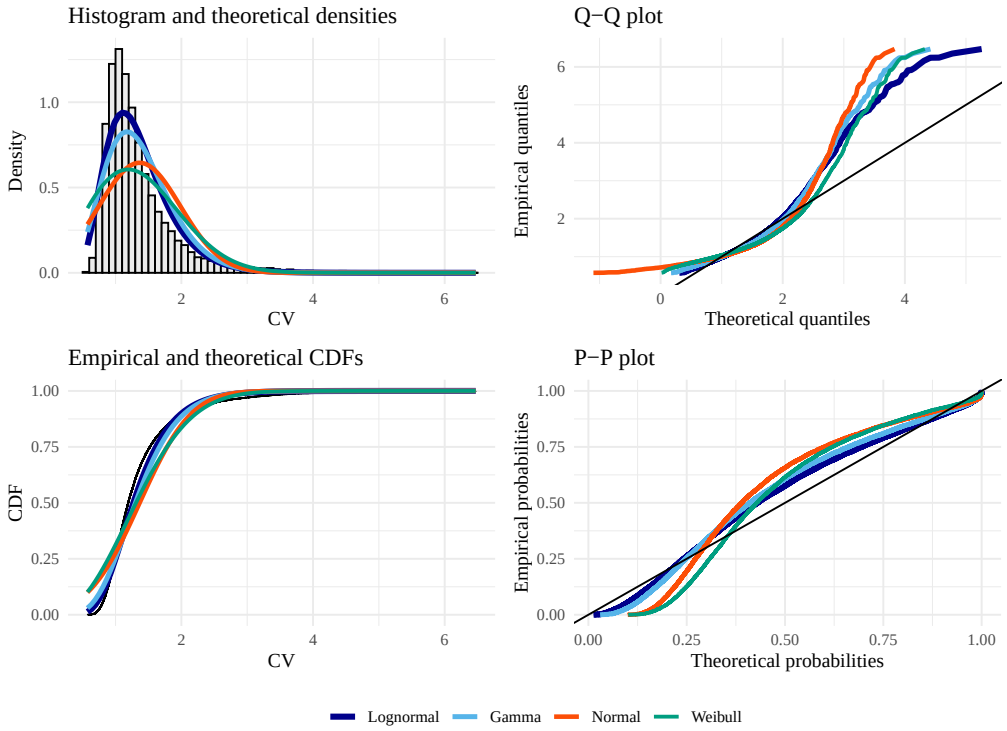


Figure 6. Goodness-of-fit plots for evaluating the best distribution with CV data from G_I^0 (under the alternative hypothesis) with $n = 49$, $L = 5$, $\mu = 1$, and $\alpha = -3$.

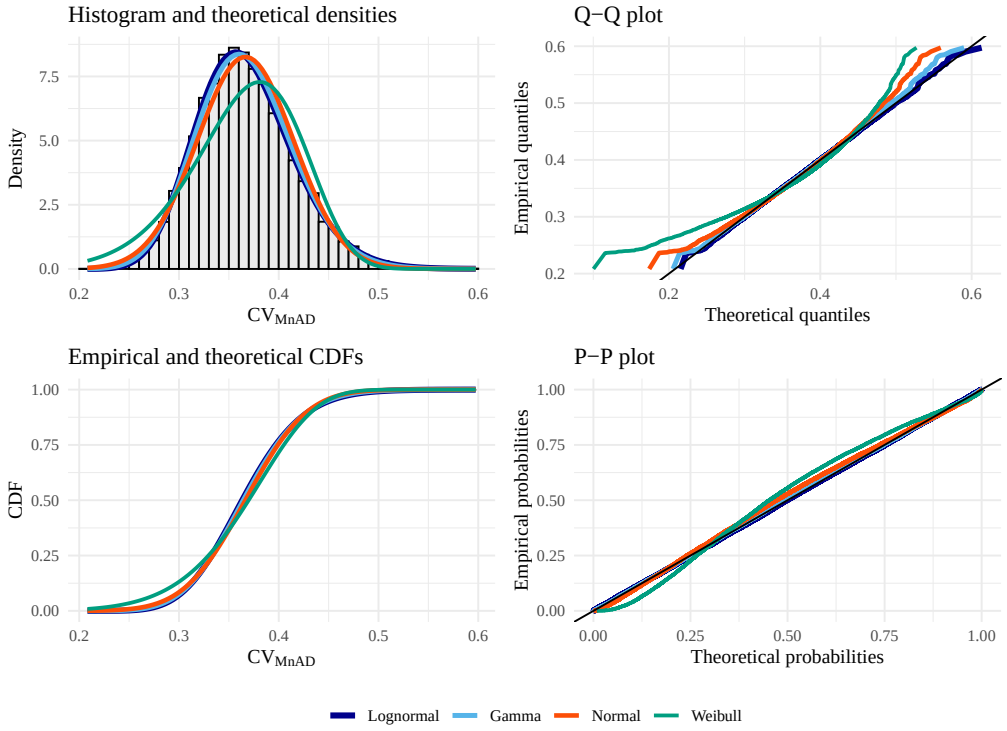


Figure 7. Goodness-of-fit plots for evaluating the best distribution with $\mathrm{CV}_{\mathrm{MnAD}}$ data from Γ_{SAR} (under the null hypothesis) with $n = 49$, $L = 5$, and $\mu = 1$.

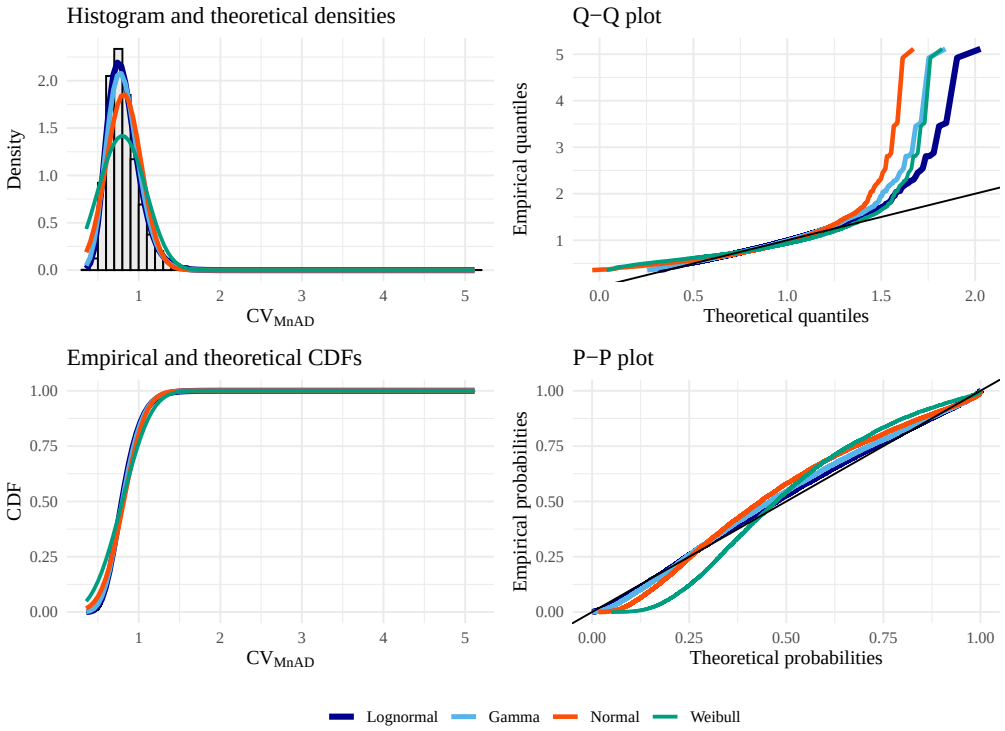


Figure 8. Goodness-of-fit plots for evaluating the best distribution with CV_{MnAD} data from G_I^0 (under the alternative hypothesis) with $n = 49$, $L = 5$, $\mu = 1$, and $\alpha = -3$.

4. Results

This section presents the simulations we performed to evaluate the proposed test statistics' performance, which was followed by applications to SAR data.

4.1. Simulated Data

Figure 9a shows the phantom with dimensions of 500×500 pixels. It was proposed by Gomez et al. [38] as a tool to assess the performance of speckle-reduction filters.

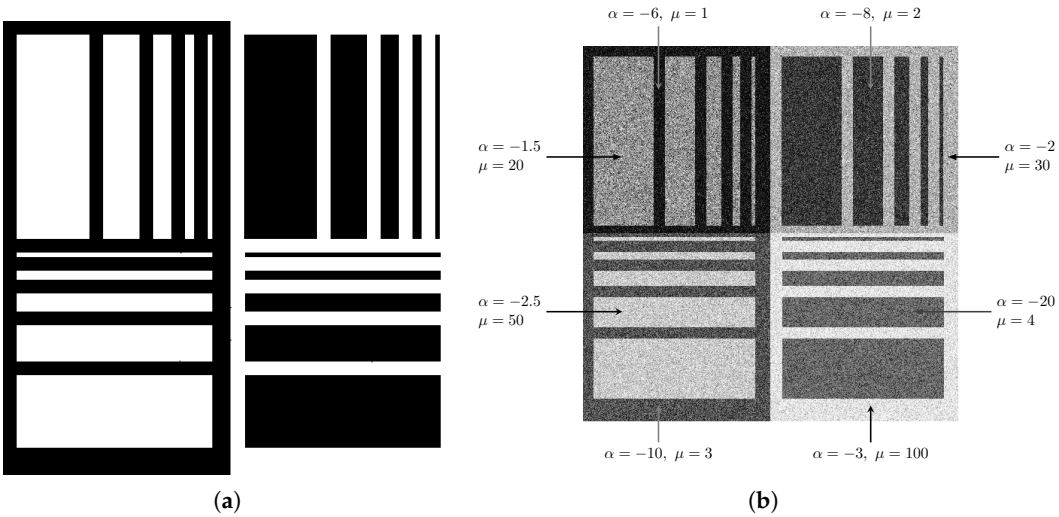


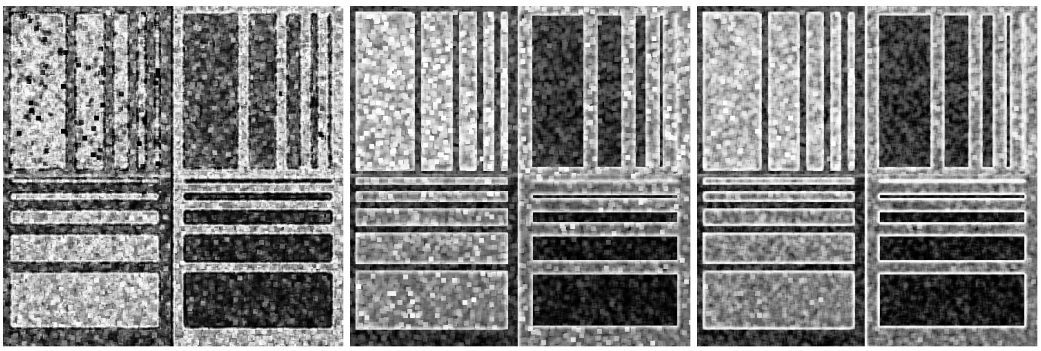
Figure 9. Synthetic dataset: (**a**) Phantom. (**b**) Simulated image, varying α and μ, with $L = 5$.

Figure 9b shows the simulated image with each small phantom displaying texture variations. The observations are independent draws from the G_I^0 distribution (5), with $L = 5$ and varying α and μ, which are annotated in the image for each quadrant. Light re-

gions correspond to textured observations (heterogeneous), while darker regions represent textureless areas (homogeneous).

The α parameter of the G_I^0 distribution is essential for interpreting texture characteristics. Values near zero greater than -3 suggest extremely textured targets, such as urban zones [39]. As the value decreases, it indicates regions with moderate texture (in the $[-6, -3]$ region), related to forest zones, while values below -6 correspond to textureless regions, such as pasture, agricultural fields, and water bodies [40].

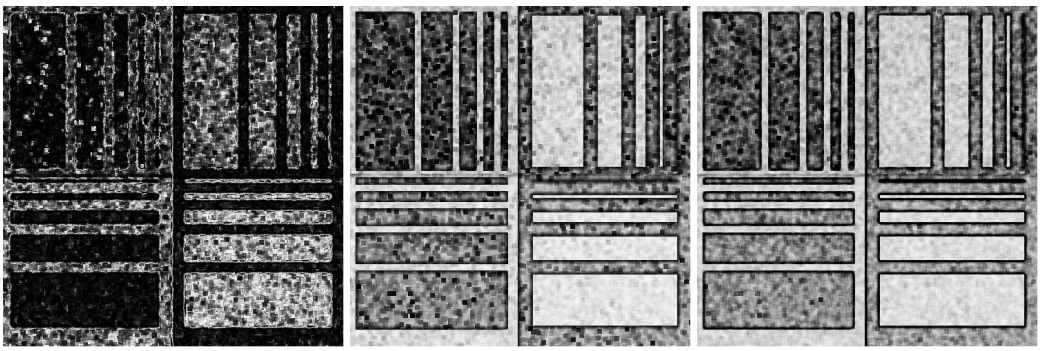
We applied the three test statistics, namely $S_{\widetilde{H}_{\mathrm{AO}}}(\boldsymbol{Z}; L)$, T_{CV}, and $T_{\mathrm{CV}_{\mathrm{MnAD}}}$, to the simulated image using local sliding windows of size 7×7, as shown in Figures 10a–c.



(**a**) (**b**) (**c**)

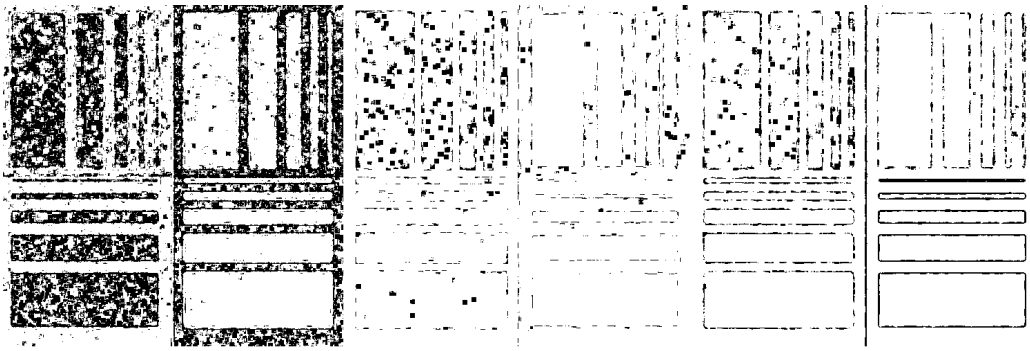
Figure 10. Results of applying the test statistics: (**a**) $S_{\widetilde{H}_{\mathrm{AO}}}(\boldsymbol{Z}; L)$, (**b**) T_{CV}, and (**c**) $T_{\mathrm{CV}_{\mathrm{MnAD}}}$.

The resulting p-values for each test are shown in Figure 11a–c. In Figure 12a–c, maps are depicted using a color table between black, gray levels, and white. All p-values above 0.05 are represented in white (indicating no evidence to reject the null hypothesis), while those below 0.05 are shown in black (indicating evidence to reject the hypothesis). We notice that the $S_{\widetilde{H}_{\mathrm{AO}}}(\boldsymbol{Z}; L)$ performs significantly better than the other tests in identifying heterogeneous areas in the simulated image.



(**a**) (**b**) (**c**)

Figure 11. Map of p-values: (**a**) $S_{\widetilde{H}_{\mathrm{AO}}}(\boldsymbol{Z}; L)$, (**b**) T_{CV}, and (**c**) $T_{\mathrm{CV}_{\mathrm{MnAD}}}$.



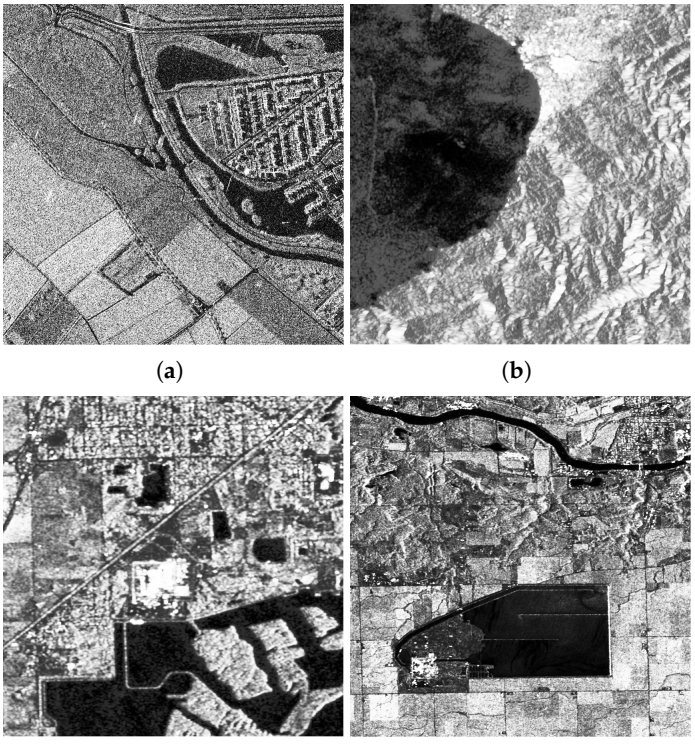
(**a**) (**b**) (**c**)

Figure 12. Results for a threshold of 0.05 of the p-value: (**a**) $S_{\widetilde{H}_{\mathrm{AO}}}(\boldsymbol{Z}; L)$, (**b**) T_{CV}, and (**c**) $T_{\mathrm{CV}_{\mathrm{MnAD}}}$.

4.2. SAR Data

We evaluated the proposed test statistics using four SAR images: one of Rotterdam, Netherlands, acquired by the TerraSAR-X satellite with Single-look Slant-range Complex (SSC) and High-resolution Spotlight-mode (HS); another of the Coast of Jalisco, Mexico; and two of Illinois, USA, acquired by the Sentinel-1B in Ground Range Detected (GRD) format, with Extra Wide-swath mode (EW) and Strip Map mode (SM). Table 9 provides detailed parameters of the selected SAR images. They contain mountainous areas, agricultural regions, water bodies, and urban areas, as shown in Figure 13a–d.

We used the number of looks L informed in the SNAP (Sentinel Application Platform) metadata: the product of azimuth and range looks. This value is close to the equivalent number of looks calculated as the ratio of the squared sample mean to the sample variance in areas with fully developed speckle.



(**a**) (**b**)

(**c**) (**d**)

Figure 13. SAR images: (**a**) Rotterdam, (**b**) Coast of Jalisco, (**c**) Illinois-Region 1, (**d**) Illinois-Region 2.

Table 9. Parameters of selected SAR images.

Site	Mission	Mode	Band	Polarization	Size	*L*	Resolution Rg/Az [m]	Acquisition Date
Rotterdam	TerraSAR-X	HS	X	HH	512 × 512	1	0.85/0.85	06-12-2018
Coast of Jalisco	Sentinel-1B	GRD EW	C	VV	512 × 512	18	40/40	29-08-2021
Illinois-Region 1	Sentinel-1B	GRD SM	C	VV	512 × 512	36	10/10	30-06-2020
Illinois-Region 2	Sentinel-1B	GRD SM	C	VV	1024 × 1024	36	10/10	28-08-2021

Figure 14a–d show the optical images obtained from Sentinel-2 L2A in true colors (composition of RGB channels) for the corresponding SAR images with acquisition dates as follows: Rotterdam (20-12-2018), Coast of Jalisco (05-09-2021), Illinois-Region 1 (25-06-2020), and Illinois-Region 2 (01-08-2021). These optical images facilitate the interpretation of the results, making it easier to distinguish between homogeneous and heterogeneous regions.

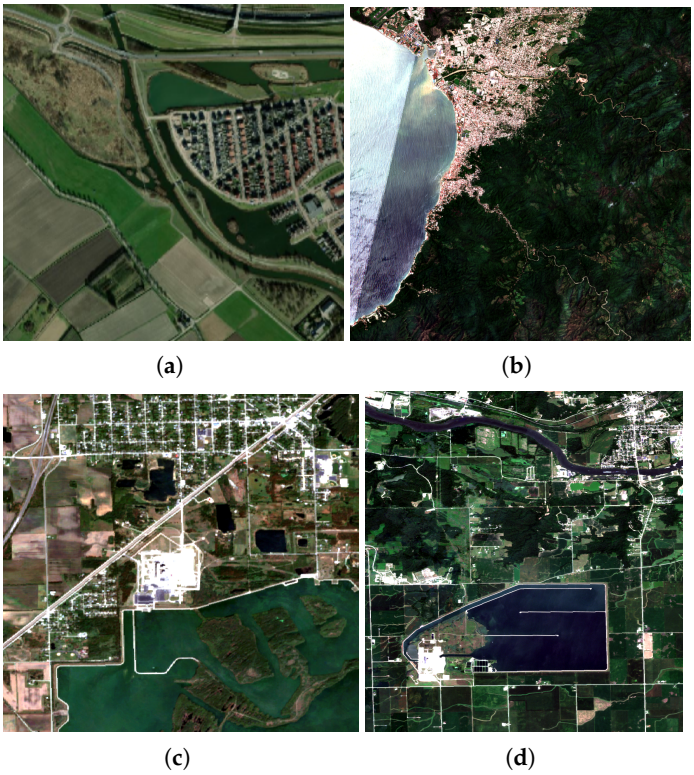


Figure 14. Optical images: (**a**) Rotterdam, (**b**) Coast Jalisco, (**c**) Illinois-Region 1, (**d**) Illinois-Region 2.

The three statistical tests are applied to the SAR images using 7 × 7 local sliding windows. This window size balances detailed local information and a sufficient number of data points, as illustrated in Figures 15–18.

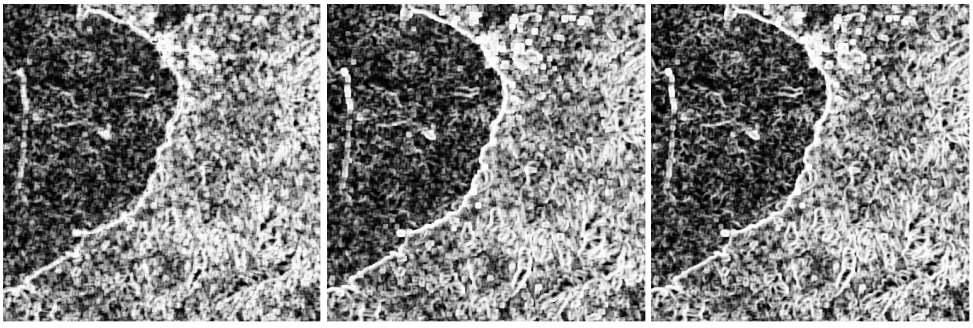
The *p*-values obtained for each test are presented in Figures 19–22, respectively.

In Figures 23–26, the maps of *p*-values composed of a linear gradient of black and white colors represent the decisions at a 5 % significance level. Dark areas represent values below 0.05, indicating evidence to reject the null hypothesis and suggesting heterogeneity in these regions. In contrast, values above 0.05 are represented as white areas, indicating no evidence to reject the fully developed speckle hypothesis.



(**a**) (**b**) (**c**)

Figure 15. Results of applying the test statistics, Rotterdam: (**a**) $S_{\widetilde{H}_{\mathrm{AO}}}(\boldsymbol{Z};L)$, (**b**) T_{CV}, and (**c**) $T_{\mathrm{CV}_{\mathrm{MnAD}}}$.



(**a**) (**b**) (**c**)

Figure 16. Results of applying the test statistics, Coast of Jalisco: (**a**) $S_{\widetilde{H}_{\mathrm{AO}}}(\boldsymbol{Z};L)$, (**b**) T_{CV}, and (**c**) $T_{\mathrm{CV}_{\mathrm{MnAD}}}$.



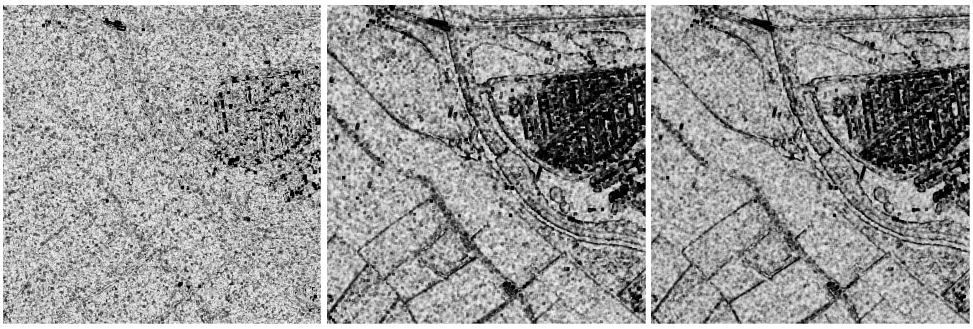
(**a**) (**b**) (**c**)

Figure 17. Results of applying the test statistics, Illinois-Region 1: (**a**) $S_{\widetilde{H}_{\mathrm{AO}}}(\boldsymbol{Z};L)$, (**b**) T_{CV}, and (**c**) $T_{\mathrm{CV}_{\mathrm{MnAD}}}$.



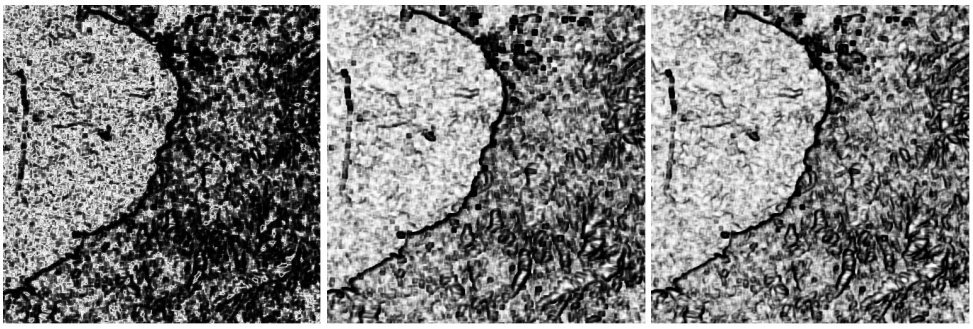
(**a**) (**b**) (**c**)

Figure 18. Results of applying the test statistics, Illinois-Region 2: (**a**) $S_{\widetilde{H}_{\mathrm{AO}}}(\boldsymbol{Z};L)$, (**b**) T_{CV}, and (**c**) $T_{\mathrm{CV}_{\mathrm{MnAD}}}$.



(**a**) (**b**) (**c**)

Figure 19. Map of p-values, Rotterdam: (**a**) $S_{\widetilde{H}_{\mathrm{AO}}}(\boldsymbol{Z}; L)$. (**b**) T_{CV}. (**c**) $T_{\mathrm{CV}_{\mathrm{MnAD}}}$.



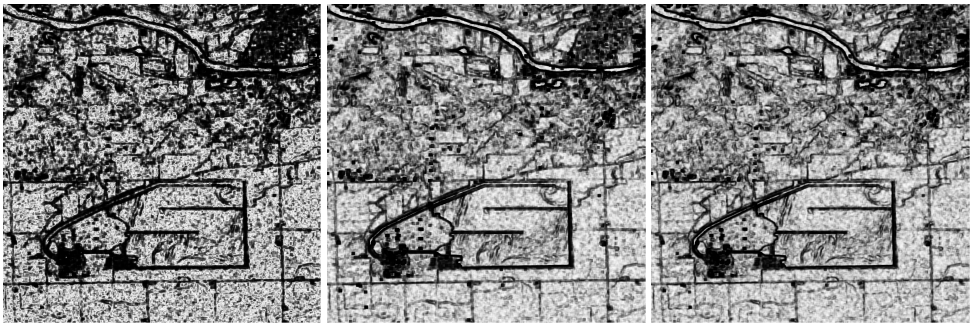
(**a**) (**b**) (**c**)

Figure 20. Map of p-values, Coast of Jalisco: (**a**) $S_{\widetilde{H}_{\mathrm{AO}}}(\boldsymbol{Z}; L)$. (**b**) T_{CV}. (**c**) $T_{\mathrm{CV}_{\mathrm{MnAD}}}$.



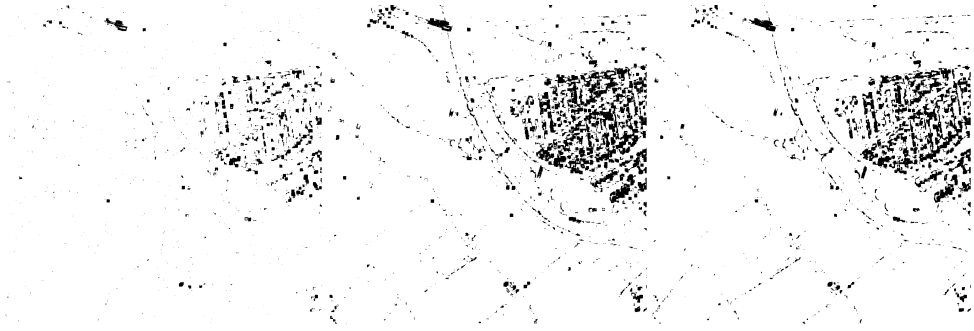
(**a**) (**b**) (**c**)

Figure 21. Map of p-values, Illinois-Region 1: (**a**) $S_{\widetilde{H}_{\mathrm{AO}}}(\boldsymbol{Z}; L)$, (**b**) T_{CV}, and (**c**) $T_{\mathrm{CV}_{\mathrm{MnAD}}}$.



(**a**) (**b**) (**c**)

Figure 22. Map of p-values, Illinois-Region 2: (**a**) $S_{\widetilde{H}_{\mathrm{AO}}}(\boldsymbol{Z}; L)$, (**b**) T_{CV}, and (**c**) $T_{\mathrm{CV}_{\mathrm{MnAD}}}$.



(**a**) (**b**) (**c**)

Figure 23. Results for a threshold of 0.05 of the p-value, Rotterdam. (**a**) $S_{\widetilde{H}_{\mathrm{AO}}}(\boldsymbol{Z}; L)$, (**b**) T_{CV}, and (**c**) $T_{\mathrm{CV}_{\mathrm{MnAD}}}$.



(**a**) (**b**) (**c**)

Figure 24. Results for a threshold of 0.05 of the p-value, Coast of Jalisco. (**a**) $S_{\widetilde{H}_{\mathrm{AO}}}(\boldsymbol{Z}; L)$, (**b**) T_{CV}, and (**c**) $T_{\mathrm{CV}_{\mathrm{MnAD}}}$.



(**a**) (**b**) (**c**)

Figure 25. Results for a threshold of 0.05 of the p-value, Illinois-Region 1. (**a**) $S_{\widetilde{H}_{\mathrm{AO}}}(\boldsymbol{Z}; L)$, (**b**) T_{CV}, and (**c**) $T_{\mathrm{CV}_{\mathrm{MnAD}}}$.



(**a**) (**b**) (**c**)

Figure 26. Results for a threshold of 0.05 of the p-value, Illinois-Region 2. (**a**) $S_{\widetilde{H}_{\mathrm{AO}}}(\boldsymbol{Z}; L)$, (**b**) T_{CV}, and (**c**) $T_{\mathrm{CV}_{\mathrm{MnAD}}}$.

Using Shannon entropy is more meaningful than using the original and robust CV to capture heterogeneity, particularly for Sentinel-1B images with a high number of looks. It is justified that the dark areas of the maps based on the T_{CV} and $T_{\mathrm{CV}_{\mathrm{MnAD}}}$ show coverage patterns similar to those reported for the $S_{\widetilde{H}_{\mathrm{AO}}}(\boldsymbol{Z}; L)$ map. This suggests that although CV-based tests may produce slightly less pronounced results than the entropy-based test, they still demonstrate a comparable ability to detect heterogeneity within SAR images.

It is noticeable that the entropy and CV-based tools predicted heterogeneity regions and boundaries where the statistical properties of texture vary. The $T_{\mathrm{CV}_{\mathrm{MnAD}}}$ test was shown to be an effective edge detector. It emerges as a robust alternative to the classical CV test, making it less susceptible to the influence of outliers and allowing it to produce more precise edges. Considering a higher significance level may increase the sensitivity to edge detection but also increase the risk of detecting false heterogeneous regions.

Additionally, assuming a 5 % threshold for p-values, in most cases, the heterogeneous regions detected by the $S_{\widetilde{H}\mathrm{AO}}(\boldsymbol{Z}; L)$ test were more extensive than those detected by the T_{CV} and $T_{\mathrm{CV}_{\mathrm{MnAD}}}$ tests. This was mainly observable in Figures 12a, 24a and 25a.

Conversely, when applying the same tests to a high-resolution TerraSAR-X image of Rotterdam, with a single look, the $S_{\widetilde{H}_{\mathrm{AO}}}(\boldsymbol{Z}; L)$ test detected less heterogeneity compared to the CV-based tests. This indicates that the performance of the entropy test depends significantly on the number of looks, performing better with a higher number of looks as in the Sentinel-1B images.

4.3. Quantitative Analysis of Test Statistics

In order to conduct a more quantitative analysis of the results, we compared the mean and standard deviation values of the different tests among selected reference areas in the Illinois-Region 2 image. These reference areas represent water, vegetation, and urban land covers, as shown in Figure 27.

We selected labeled polygons (water, vegetation, urban) and conducted 100 sampling iterations with replacement from each category, using window sizes of 11×11 pixels. For each sample, we applied the corresponding test statistic. Finally, we computed the mean and standard deviation of the results obtained from the 100 samples.

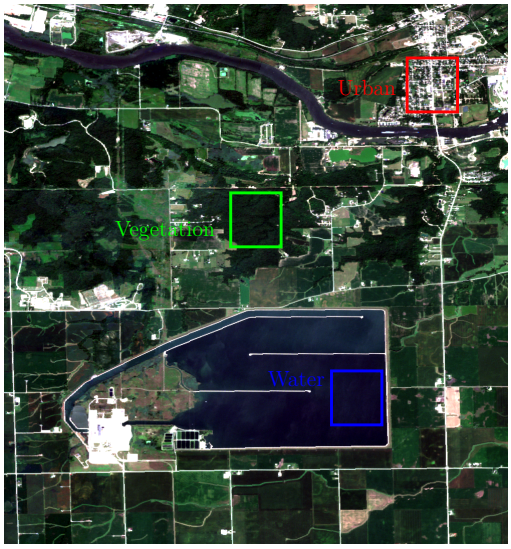


Figure 27. Image of Illinois-Region 2 with reference samples.

Table 10 presents the comparison of the mean and standard deviation values for the three tests across the reference areas.

Table 10. Analysis of test statistics for different areas of reference.

Area of Reference	Test Statistic	Mean	SD
Water	$S_{\widetilde{H}_{\mathrm{AO}}}(\mathbf{Z};L)$	0.05029	0.15415
	T_{CV}	0.15827	0.02584
	$T_{\mathrm{CV}_{\mathrm{MnAD}}}$	0.13013	0.02183
Vegetation	$S_{\widetilde{H}_{\mathrm{AO}}}(\mathbf{Z};L)$	0.36482	0.28489
	T_{CV}	0.29421	0.10957
	$T_{\mathrm{CV}_{\mathrm{MnAD}}}$	0.24501	0.09829
Urban	$S_{\widetilde{H}_{\mathrm{AO}}}(\mathbf{Z};L)$	0.82970	0.21910
	T_{CV}	0.56846	0.33938
	$T_{\mathrm{CV}_{\mathrm{MnAD}}}$	0.47176	0.29486

Based on the analysis, $S_{\widetilde{H}_{\mathrm{AO}}}(\mathbf{Z};L)$ appears to be the most sensitive test for classification purposes, because it shows the largest distinction in mean values between the different land cover types, indicating it is better at differentiating between homogeneous and heterogeneous areas. However, the CV and $\mathrm{CV}_{\mathrm{MnAD}}$ test are also reliable with a lower variability, making them good candidates depending on the specific application.

5. Conclusions

This article provides a practical and theoretical answer to the following physical question: how does on detect heterogeneity in SAR images, assuming that the SAR intensity follows the Γ_{SAR} model? To this end, we proposed three novel hypothesis tests: one from the Shannon entropy and two from the variation coefficient variants. The performance of our proposals was evaluated using a Monte Carlo study. The results showed that they were conservative in estimating the probability of a Type I error (false alarm rate) and the test power (probability of detection), which increases with sample size. An application to four recent SAR images was performed. The results showed that the Shannon entropy-based test was more robust than the CV-based tests for Sentinel-1B images. For high-resolution images with a single look, such as the TerraSAR-X image, the classical CV test was more effective in detecting heterogeneous regions. In addition, all tests could recognize images with different textures and identify edges where the texture type changes.

Despite presenting the results of using the estimators as local filters, we suggest using them in specific samples that visibly contain only one type of land use or land cover. This type of analysis can assist users in selecting appropriate training samples for classification purposes.

Supplementary Materials: This article was written in Rmarkdown and is fully reproducible. The code and data are accessible at https://github.com/rjaneth/identifying-heterogeneity-in-sar-data-with-new-test-statistics (accessed on 30 April 2024).

Author Contributions: All authors (A.C.F., J.A. and A.D.C.N.) discussed the results and contributed to the research. All authors have read and agreed to the published version of the manuscript.

Funding: This research received no external funding.

Data Availability Statement: The Sentinel-1 images are made publicly available by the European Space Agency via Copernicus Data Space Ecosystem at https://dataspace.copernicus.eu/ (accessed on 24 April 2024).

Acknowledgments: The author J.A. would like to thank the Coordenação de Aperfeiçoamento de Pessoal de Nível Superior (CAPES) and the Fundação de Amparo à Ciência e Tecnologia de Pernambuco (FACEPE) for their support.

Conflicts of Interest: The authors declare no conflicts of interest.

Appendix A. Limit Behavior of $H_{G_I^0}$ as $\alpha \to -\infty$

To verify that $H_{G_I^0}(\mu, \alpha, L)$ converges to $H_{\Gamma_{\text{SAR}}}(L, \mu)$ as $\alpha \to -\infty$, we show that the additional terms in $H_{G_I^0}$ cancel in the limit.

The Shannon entropy for the G_I^0 distribution is given by

$$H_{G_I^0}(\mu, \alpha, L) = H_{\Gamma_{\text{SAR}}}(L, \mu) - \ln\Gamma(L-\alpha) + (L-\alpha)\psi^{(0)}(L-\alpha) - (1-\alpha)\psi^{(0)}(-\alpha) + \ln(-1-\alpha) + \ln\Gamma(-\alpha) - L.$$

We aim to show that

$$\lim_{\alpha\to-\infty} H_{G_I^0}(\mu, \alpha, L) = H_{\Gamma_{\text{SAR}}}(L, \mu).$$

The additional terms in $H_{G_I^0}$ compared to $H_{\Gamma_{\text{SAR}}}$ are

$$\lim_{\alpha\to-\infty}\Big[-\ln\Gamma(L-\alpha) + (L-\alpha)\psi^{(0)}(L-\alpha) - (1-\alpha)\psi^{(0)}(-\alpha) + \ln(-1-\alpha) + \ln\Gamma(-\alpha)\Big] - L. \tag{A1}$$

For $L = 1$, this becomes

$$\lim_{\alpha\to-\infty}\Bigg[\underbrace{-\ln\Gamma(1-\alpha) + \ln(-1-\alpha) + \ln\Gamma(-\alpha)}_{A} + \underbrace{(1-\alpha)\psi^{(0)}(1-\alpha) - (1-\alpha)\psi^{(0)}(-\alpha)}_{B}\Bigg] - 1. \tag{A2}$$

Simplifying A and B

$$A = \ln\frac{(-1-\alpha)\Gamma(-\alpha)}{\Gamma(1-\alpha)} = \ln\frac{(-1-\alpha)\Gamma(-\alpha)}{-\alpha\Gamma(-\alpha)} = \ln\frac{-1-\alpha}{-\alpha} = \ln\left(1+\frac{1}{\alpha}\right).$$

$$\begin{aligned} B = (1-\alpha)\Big[\psi^{(0)}(1-\alpha) - \psi^{(0)}(-\alpha)\Big] &= (1-\alpha)\Bigg[\psi^{(0)}\underbrace{(1-\alpha-1) + \frac{1}{1-\alpha-1}}_{\text{Because } \psi^{(0)}(x+1)=\psi^{(0)}(x)+\frac{1}{x}} - \psi^{(0)}(-\alpha)\Bigg] \\ &= (1-\alpha)\left[\psi^{(0)}(-\alpha) - \frac{1}{\alpha} - \psi^{(0)}(-\alpha)\right] \\ &= -\frac{1}{\alpha} + 1. \end{aligned}$$

Replacing A and B into (A2) and taking the limit, we obtain

$$\underbrace{\lim_{\alpha\to-\infty}\ln\left(1+\frac{1}{\alpha}\right)}_{\text{approaches 0}} - \underbrace{\lim_{\alpha\to-\infty}\frac{1}{\alpha}}_{\text{approaches 0}} + \lim_{\alpha\to-\infty} 1 - 1 = 0.$$

For the general case for $L > 1$, we use Stirling's approximation for large z:

$$\Gamma(z) \sim \sqrt{2\pi z}\left(\frac{z}{e}\right)^z,$$

and

$$\psi^{(0)}(z) \sim \ln(z) - \frac{1}{2z}.$$

Therefore, the terms of Equation (A1) approximate to

$$-\ln\Gamma(L-\alpha) \sim -\frac{1}{2}\ln\left(2\pi(L-\alpha)\right) - (L-\alpha)\ln(L-\alpha) + (L-\alpha),$$
$$(L-\alpha)\psi^{(0)}(L-\alpha) \sim (L-\alpha)\left[\ln(L-\alpha) - \frac{1}{2(L-\alpha)}\right] \sim (L-\alpha)\ln(L-\alpha) - \frac{1}{2},$$
$$-(1-\alpha)\psi^{(0)}(-\alpha) \sim -(1-\alpha)\ln(-\alpha) - \frac{1-\alpha}{2\alpha},$$

and

$$\ln\Gamma(-\alpha) \sim \frac{1}{2}\ln(-2\pi\alpha) - \alpha\ln(-\alpha) + \alpha.$$

Then, replacing these terms in (A1), we obtain

$$\lim_{\alpha\to-\infty}\Bigg[-\frac{1}{2}\ln\left(2\pi(L-\alpha)\right) - L\ln(L-\alpha) + \alpha\ln(L-\alpha) + L - \alpha + L\ln(L-\alpha) - \alpha\ln(L-\alpha)$$
$$-\frac{1}{2} - \ln(-\alpha) + \alpha\ln(-\alpha) - \frac{1-\alpha}{2\alpha} + \ln(-1-\alpha) + \frac{1}{2}\ln(-2\pi\alpha) - \alpha\ln(-\alpha) + \alpha\Bigg] - L.$$

We, then, simplify the expression to

$$\lim_{\alpha\to-\infty}\left[-\frac{1}{2}\ln\left(2\pi(L-\alpha)\right) + L - \frac{1}{2} - \ln(-\alpha) - \frac{1-\alpha}{2\alpha} + \ln\left(-(1+\alpha)\right) + \frac{1}{2}\ln(-2\pi\alpha)\right] - L.$$

We now group terms:

$$\lim_{\alpha\to-\infty}\left[\frac{1}{2}\ln\frac{-\alpha}{L-\alpha} + L - \frac{1}{2} + \frac{\alpha-1}{2\alpha} + \ln\frac{1+\alpha}{\alpha}\right] - L = \frac{1}{2}\ln 1 + L - \frac{1}{2} + \frac{1}{2} + \ln 1 - L = 0.$$

Therefore

$$\lim_{\alpha\to-\infty} H_{G_I^0}(\mu,\alpha,L) = H_{\Gamma_{\mathrm{SAR}}}(L,\mu),$$

which concludes the proof.

Appendix B. Computational Information

We used a MacBook Pro, 14-inch 2021 computer with Apple M1 Max chip, 64 GB of memory, running macOS Sonoma 14.5 operating system, sourced in New Zealand. All the computational developments, including the text, were produced with RMarkdown v.2.27, RStudio v. 2024.04.1+748, and R v. 4.4.0.

References

1. Moreira, A.; Prats-Iraola, P.; Younis, M.; Krieger, G.; Hajnsek, I.; Papathanassiou, K.P. A tutorial on synthetic aperture radar. *IEEE Geosci. Remote Sens. Mag.* **2013**, *1*, 6–43. [CrossRef]
2. Mu, Y.; Huang, B.; Pan, Z.; Yang, H.; Hou, G.; Duan, J. An Enhanced High-Order Variational Model Based on Speckle Noise Removal With G^0 Distribution. *IEEE Access* **2019**, *7*, 104365–104379. [CrossRef]
3. Argenti, F.; Lapini, A.; Bianchi, T.; Alparone, L. A Tutorial on Speckle Reduction in Synthetic Aperture Radar Images. *IEEE Geosci. Remote Sens. Mag.* **2013**, *1*, 6–35. [CrossRef]
4. Ferreira, J.d.A.; Nascimento, A.D.C. Shannon Entropy for the $\mathcal{G}_I^0$ Model: A New Segmentation Approach. *IEEE J. Sel. Top. Appl. Earth Obs. Remote Sens.* **2020**, *13*, 2547–2553.
5. Pressé, S.; Ghosh, K.; Lee, J.; Dill, K.A. Principles of maximum entropy and maximum caliber in statistical physics. *Rev. Mod. Phys.* **2013**, *85*, 1115–1141. [CrossRef]
6. Mohammad-Djafari, A. Entropy, Information Theory, Information Geometry and Bayesian Inference in Data, Signal and Image Processing and Inverse Problems. *Entropy* **2015**, *17*, 3989–4027. [CrossRef]

7. Avval, T.G.; Moeini, B.; Carver, V.; Fairley, N.; Smith, E.F.; Baltrusaitis, J.; Fernandez, V.; Tyler, B.J.; Gallagher, N.; Linford, M.R. The Often-Overlooked Power of Summary Statistics in Exploratory Data Analysis: Comparison of Pattern Recognition Entropy (PRE) to Other Summary Statistics and Introduction of Divided Spectrum-PRE (DS-PRE). *J. Chem. Inf. Model.* **2021**, *61*, 4173–4189. [CrossRef] [PubMed]
8. Nascimento, A.D.C.; Horta, M.M.; Frery, A.C.; Cintra, R.J. Comparing Edge Detection Methods Based on Stochastic Entropies and Distances for PolSAR Imagery. *IEEE J. Sel. Top. Appl. Earth Obs. Remote Sens.* **2014**, *7*, 648–663. [CrossRef]
9. Nascimento, A.D.C.; Frery, A.C.; Cintra, R.J. Detecting Changes in Fully Polarimetric SAR Imagery With Statistical Information Theory. *IEEE Trans. Geosci. Remote Sens.* **2019**, *57*, 1380–1392. [CrossRef]
10. Shannon, C.E. A Mathematical Theory of Communication. *Bell Syst. Tech. J.* **1948**, *27*, 379–423. [CrossRef]
11. Wieczorkowski, R.; Grzegorzewski, P. Entropy estimators-improvements and comparisons. *Comm. Statist. Simul. Comput.* **1999**, *28*, 541–567. [CrossRef]
12. Zamanzade, E.; Arghami, N.R. Testing normality based on new entropy estimators. *J. Stat. Comput. Simul.* **2012**, *82*, 1701–1713. [CrossRef]
13. Alizadeh Noughabi, H. A new estimator of entropy and its application in testing normality. *J. Stat. Comput. Simul.* **2010**, *80*, 1151–1162. [CrossRef]
14. Subhash, S.; Sunoj, S.M.; Sankaran, P.G.; Rajesh, G. Nonparametric estimation of quantile-based entropy function. *Commun. Stat. Simul. Comput.* **2021**, *52*, 1805–1821. [CrossRef]
15. Pearson, K.; Henrici, O.M.F.E. VII. Mathematical contributions to the theory of evolution.—III. Regression, heredity, and panmixia. *Philos. Trans. R. Soc. Lond. Ser. A Contain. Pap. Math. Phys. Character* **1896**, *187*, 253–318.
16. Walter A. Hendricks, K.W.R. The Sampling Distribution of the Coefficient of Variation. *Ann. Math. Stat.* **1936**, *7*, 129–132.
17. Tian, L. Inferences on the common coefficient of variation. *Stat. Med.* **2005**, *24*, 2213–2220. [CrossRef] [PubMed]
18. Subrahmanya Nairy, K.; Aruna Rao, K. Tests of Coefficients of Variation of Normal Population. *Commun. Stat.-Simul. Comput.* **2003**, *32*, 641–661. [CrossRef]
19. Chankham, W.; Niwitpong, S.A.; Niwitpong, S. The Simultaneous Confidence Interval for the Ratios of the Coefficients of Variation of Multiple Inverse Gaussian Distributions and Its Application to PM2.5 Data. *Symmetry* **2024**, *16*, 331. [CrossRef]
20. Banik, S.; Kibria, B.M.G. Estimating the Population Coefficient of Variation by Confidence Intervals. *Commun. Stat.-Simul. Comput.* **2011**, *40*, 1236–1261. [CrossRef]
21. Ulaby, F.; Kouyate, F.; Brisco, B.; Williams, T.H. Textural Information in SAR Images. *IEEE Trans. Geosci. Remote Sens.* **1986**, *GE-24*, 235–245. [CrossRef]
22. Touzi, R.; Lopes, A.; Bousquet, P. A statistical and geometrical edge detector for SAR images. *IEEE Trans. Geosci. Remote Sens.* **1988**, *26*, 764–773. [CrossRef]
23. Frery, A.C.; Muller, H.J.; Yanasse, C.; Sant'Anna, S. A model for extremely heterogeneous clutter. *IEEE Trans. Geosci. Remote Sens.* **1997**, *35*, 648–659. [CrossRef]
24. Cassetti, J.; Delgadino, D.; Rey, A.; Frery, A.C. Entropy Estimators in SAR Image Classification. *Entropy* **2022**, *24*, 509. [CrossRef] [PubMed]
25. Nascimento, A.D.C.; Cintra, R.J.; Frery, A.C. Hypothesis Testing in Speckled Data With Stochastic Distances. *IEEE Trans. Geosci. Remote Sens.* **2010**, *48*, 373–385. [CrossRef]
26. Vasicek, O. A test for normality based on sample entropy. *J. R. Stat. Soc. Ser. B Methodol.* **1976**, *38*, 54–59. [CrossRef]
27. Correa, J.C. A new estimator of entropy. *Commun. Stat.–Theory Methods* **1995**, *24*, 2439–2449. [CrossRef]
28. Al-Omari, A.I.; Haq, A. Novel entropy estimators of a continuous random variable. *Int. J. Model. Simul. Sci. Comput.* **2019**, *10*, 1950004. [CrossRef]
29. Ebrahimi, N.; Pflughoeft, K.; Soofi, E.S. Two measures of sample entropy. *Stat. Probab.* **1994**, *20*, 225–234. [CrossRef]
30. Al-Omari, A.I. Estimation of entropy using random sampling. *J. Comput. Appl. Math.* **2014**, *261*, 95–102. [CrossRef]
31. Michelucci, U.; Venturini, F. Estimating Neural Network's Performance with Bootstrap: A Tutorial. *Mach. Learn. Knowl. Extr.* **2021**, *3*, 357–373. [CrossRef]
32. Ospina, R.; Marmolejo-Ramos, F. Performance of Some Estimators of Relative Variability. *Front. Appl. Math. Stat.* **2019**, *5*, 43. [CrossRef]
33. Chaubey, Y.P.; Singh, M.; Sen, D. Symmetrizing and Variance Stabilizing Transformations of Sample Coefficient of Variation from Inverse Gaussian Distribution. *Sankhya B* **2017**, *79*, 217–246. [CrossRef]
34. Takagi, K.; Kumagai, S.; Matsunaga, I.; Kusaka, Y. Application of inverse Gaussian distribution to occupational exposure data. *Ann. Occup. Hyg.* **1997**, *41*, 505–514. [CrossRef]
35. Whitmore, G.; Yalovsky, M. A normalizing logarithmic transformation for inverse Gaussian random variables. *Technometrics* **1978**, *20*, 207–208. [CrossRef]
36. Burnham, K.P.; Anderson, D.R. Multimodel Inference: Understanding AIC and BIC in Model Selection. *Sociol. Methods Res.* **2004**, *33*, 261–304. [CrossRef]
37. Dziak, J.J.; Coffman, D.L.; Lanza, S.T.; Li, R.; Jermiin, L.S. Sensitivity and specificity of information criteria. *Briefings Bioinform.* **2019**, *21*, 553–565. [CrossRef]
38. Gomez, L.; Alvarez, L.; Mazorra, L.; Frery, A.C. Fully PolSAR image classification using machine learning techniques and reaction-diffusion systems. *Neurocomputing* **2017**, *255*, 52–60. [CrossRef]

39. Frery, A.C.; Gambini, J. Comparing samples from the $\mathcal{G}^0$ distribution using a geodesic distance. *TEST* **2019**, *29*, 359–378. [CrossRef]
40. Neto, J.F.S.R.; Rodrigues, F.A.A. Improving Log-Cumulant-Based Estimation of Heterogeneity Information in SAR Imagery. *IEEE Geosci. Remote Sens. Lett.* **2023**, *20*, 1–5. [CrossRef]

Disclaimer/Publisher's Note: The statements, opinions and data contained in all publications are solely those of the individual author(s) and contributor(s) and not of MDPI and/or the editor(s). MDPI and/or the editor(s) disclaim responsibility for any injury to people or property resulting from any ideas, methods, instructions or products referred to in the content.